Inviscid helical magnetorotational instability in cylindrical Taylor-Couette flow

Priede, J.

Inviscid helical magnetorotational instability in cylindrical Taylor-Couette flow

Jānis Priede*

Applied Mathematics Research Centre, Coventry University, Coventry CV1 5FB, United Kingdom

(Received 19 August 2011; published 19 December 2011)

This paper presents the analysis of axisymmetric helical magnetorotational instability (HMRI) in the inviscid limit, which is relevant for astrophysical conditions. The inductionless approximation defined by zero magnetic Prandtl number is adopted to distinguish the HMRI from the standard MRI in the cylindrical Taylor-Couette flow subject to a helical magnetic field. Using a Chebyshev collocation method convective and absolute instability thresholds are computed in terms of the Elsasser number for a fixed ratio of inner and outer radii $\lambda = 2$ and various ratios of rotation rates and helicities of the magnetic field. It is found that the extension of self-sustained HMRI modes beyond the Rayleigh limit does not reach the astrophysically relevant Keplerian rotation profile not only in the narrow- but also in the finite-gap approximation. The Keppler limit can be attained only by the convective HMRI mode provided that the boundaries are perfectly conducting. However, this mode requires not only a permanent external excitation to be observable but also has a long axial wavelength, which is not compatible with limited thickness of astrophysical accretion disks.

DOI: 10.1103/PhysRevE.84.066314 PACS number(s): 47.20.Qr, 47.65.−d, 95.30.Lz

I. INTRODUCTION

The magnetorotational instability (MRI) is a mechanism by which the magnetic field can destabilize a hydrodynamically stable flow of a conducting fluid without altering its velocity distribution. The MRI was first discovered theoretically in cylindrical Taylor-Couette (TC) flow of perfectly conducting fluid subject to an axial magnetic field [1,2]. Three decades later, Balbus and Hawley [3] suggested that the MRI may account for the fast formation of stars by driving turbulent transport of angular momentum in accretion disks. This proposition has triggered not only numerous theoretical studies [4] but also several attempts to reproduce the MRI in the laboratory [5,6]. A major challenge to such experiments is posed by the parameter known as the magnetic Reynolds number Rm, which is required to be at least ∼10 for the MRI to set in. For a typical liquid metal, characterized by a small magnetic Prandtl number $\mathrm{Pm} \sim 10^{-5}$–10^{-6}, this translates into a large hydrodynamic Reynolds number $\mathrm{Re} = \mathrm{Rm}/\mathrm{Pm} \sim 10^6$–$10^7$ [7]. At such large Reynolds numbers, the flow on which the MRI is expected to develop may become turbulent due to purely hydrodynamic instabilities [5].

A way to circumvent this problem was proposed by Hollerbach and Rüdiger [8], who suggested that a magnetorotational-type instability can take place in cylindrical TC flow at $\mathrm{Re} \sim 10^3$ when the imposed magnetic field is helical rather than purely axial as for the standard MRI (SMRI). An instability resembling this new type helical MRI (HMRI) was shortly thereafter observed in the PROMISE experiment [9–11]. These observations were disputed by Liu *et al.* [12], who found no such instability in their inviscid theoretical analysis of finite length cylinders with insulating end caps. Subsequently, the observed phenomenon was conjectured to be a transient growth rather than a self-sustained instability [13–15]. This proposition was, in turn, opposed by Priede and Gerbeth [16], who showed that there is not only a convective but also an absolute HMRI threshold. Thus a self-sustained HMRI can experimentally be observed in a system of sufficiently large axial extension. However, the comparison with the experimental results revealed that the HMRI has been observed slightly beyond the range of its absolute instability, where it is expected according to ideal TC flow model. This discrepancy implies a deviation of the real base flow from the TC one, which may be caused by the end effects. One such end effect disturbing the base flow in the original PROMISE experiment was due to the copper end cap, which allowed radial electric current to connect over the liquid gap between the cylinders [17]. This flaw was corrected in the modified PROMISE experiment, where an insulating end cap was used, which, in order to reduce the Ekman pumping, was split into two separately rotating rings [18,19]. Although the instability appeared much sharper in the modified setup than in the original one, its nature may still be questionable. Uncertainty is due to the virtually unknown hydrodynamic stability limit of the real base flow, whose deviation from ideal TC flow was significant and practically unavoidable in the experiment. Without knowing the actual hydrodynamic stability limit it is practically impossible to distinguish the HMRI from a magnetically modified Taylor vortex flow [17].

Regardless of the experimental reproducibility, the HMRI is also of a questionable astrophysical relevance. Using a WKB analysis Liu *et al.* [12] showed that however the HMRI is able to destabilize centrifugally stable velocity distributions, it does not reach up to the astrophysically relevant Keplerian rotation profile. This claim was doubted by Rüdiger and Hollerbach [20], who pointed out that according to the numerical results for the TC flow in a finite-width gap [21], the HMRI can apparently reach the Keplerian rotation profile provided that at least one of the boundaries is sufficiently conducting. However, it is important to note that this conclusion concerns only the convective HMRI, which is not generally self-sustained and requires an external excitation to be effective. No destabilizing effect due to conducting boundaries was observed for the absolute instability threshold [16]. Although the extension of the absolute HMRI beyond the Rayleigh line was found to increase with the strength and helicity of the magnetic field, the previous study was unable to conclude whether the Keplerian

*j.priede@coventry.ac.uk

velocity profile is attainable. The problem was the excessive numerical resolution required for the thin boundary layers developing in strong magnetic field. However, the HMRI does not appear to be related with the boundary layers, whose main function is to satisfy the no-slip boundary condition imposed by the viscosity. These redundant boundary layers can be eliminated by ignoring the viscosity, which appears to be insignificant for astrophysical conditions. In this paper, fluid is considered not only inviscid but also highly electrically resistive. It means that the magnetic Prandtl number is assumed to be zero regardless of the viscosity, which corresponds to the inductionless approximation [21].

The aim of the present work is to investigate numerically whether the astrophysically relevant Keplerian rotation profile can be attained by inviscid HMRI in cylindrical TC flow when a finite-width annulus is considered. The obtained results show that only convective HMRI mode can reach the Kepler limit provided that the boundaries are perfectly conducting. However, this mode requires not only a permanent external excitation to be observable but also has a long wavelength, which is incompatible with limited thickness of accretion disks. The absolute HMRI as well as the convective one at insulating boundaries are found to obey the Liu limit also for a finite-width annulus. This is because the maximum extension of the HMRI beyond the Rayleigh line is attained when the magnetic field is nearly azimuthal, which results in a short-wave instability as in the local WKB approximation.

The paper is organized as follows. In Sec. II the problem is formulated. The local WKB-type solution for a narrow gap is revisited in Sec. III. Section IV presents numerical results concerning the convective and absolute HMRI thresholds for both insulating and perfectly conducting boundaries. The paper is concluded with a summary of results in Sec. V.

II. PROBLEM FORMULATION

Consider an incompressible inviscid fluid of electrical conductivity σ filling the gap between two infinite concentric cylinders with the inner radius R_i and the outer radius R_o rotating with the angular velocities Ω_i and Ω_o, respectively, in the presence of an externally imposed steady magnetic field $\mathbf{B}_0 = B_\phi \mathbf{e}_\phi + B_z \mathbf{e}_z$ with axial and azimuthal components $B_z = B_0$ and $B_\phi = \beta B_0 R_i/r$ in the cylindrical coordinates (r,ϕ,z), where β is a dimensionless parameter characterizing the geometrical helicity of the magnetic field (see Fig. 1). The induced magnetic field is assumed to be negligible relative to the imposed one, which corresponds to the inductionless approximation. The velocity of inviscid fluid flow $\mathbf{v}$ is governed by Euler equation with electromagnetic body force,

$$\frac{\partial \mathbf{v}}{\partial t} + (\mathbf{v}\cdot\nabla)\mathbf{v} = -\rho^{-1}(\nabla p + \mathbf{j}\times\mathbf{B}_0), \tag{1}$$

where the induced current follows from Ohm's law for moving medium,

$$\mathbf{j} = \sigma(\mathbf{E} + \mathbf{v}\times\mathbf{B}_0). \tag{2}$$

In addition, we assume the characteristic time of velocity variation to be much longer than the magnetic diffusion time $\tau_0 \gg \tau_m = \mu_0\sigma L^2$, which leads to the quasistationary approximation, according to which $\nabla\times\mathbf{E} = 0$ and $\mathbf{E} = -\nabla\Phi$,

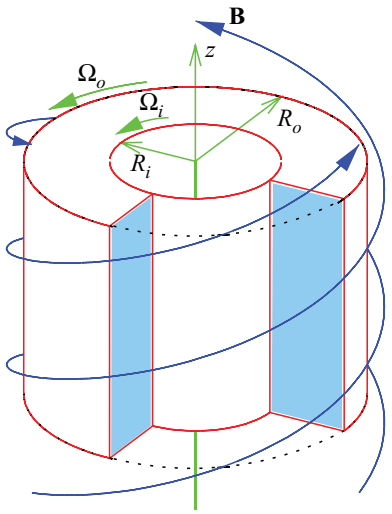

FIG. 1. (Color online) Sketch of the formulation of the problem.

where Φ is the electrostatic potential [22]. Mass and charge conservation imply $\nabla\cdot\mathbf{v} = \nabla\cdot\mathbf{j} = 0$.

As long as the viscosity is not exactly zero, the problem admits a base state with a purely azimuthal velocity distribution $\mathbf{v}_0(r) = \mathbf{e}_\phi v_0(r)$, where the velocity profile

$$v_0(r) = r\frac{\Omega_o R_o^2 - \Omega_i R_i^2}{R_o^2 - R_i^2} + \frac{1}{r}\frac{\Omega_o - \Omega_i}{R_o^{-2} - R_i^{-2}}$$

is independent of the viscosity and thus holds also in the inviscid limit.

Note that the base flow is not affected by the magnetic field because the latter gives rise only to the electrostatic potential $\Phi_0(r) = B_0\int v_0(r)dr$, whose gradient compensates the induced electric field so that there is no current in the base state ($\mathbf{j}_0 = 0$). However, current may be induced in the perturbed state,

$$\begin{Bmatrix} \mathbf{v}, & p \\ \mathbf{j}, & \Phi \end{Bmatrix}(\mathbf{r},t) = \begin{Bmatrix} \mathbf{v}_0, & p_0 \\ \mathbf{j}_0, & \Phi_0 \end{Bmatrix}(r) + \begin{Bmatrix} \mathbf{v}_1, & p_1 \\ \mathbf{j}_1, & \Phi_1 \end{Bmatrix}(\mathbf{r},t),$$

where $\mathbf{v}_1$, p_1, $\mathbf{j}_1$, and Φ_1 are small-amplitude perturbations for which Eqs. (1) and (2) after linearization take the form

$$\frac{\partial \mathbf{v}_1}{\partial t} + (\mathbf{v}_1\cdot\nabla)\mathbf{v}_0 + (\mathbf{v}_0\cdot\nabla)\mathbf{v}_1 = -\rho^{-1}(\nabla p_1 + \mathbf{j}_1\times\mathbf{B}_0),$$
$$\mathbf{j}_1 = \sigma(-\nabla\Phi_1 + \mathbf{v}_1\times\mathbf{B}_0). \tag{3}$$

In the following, we focus on the axisymmetric perturbations, which are typically much more unstable than the nonaxisymmetric ones [23]. The nonaxisymmetric HMRI modes recently found by Hollerbach, Teeluck, and Rüdiger [24] in purely azimuthal magnetic field lay outside the scope of this study. For axisymmetric perturbations, the solenoidality constraints are satisfied by meridional stream functions for fluid flow and electric current as

$$\mathbf{v} = v\mathbf{e}_\phi + \nabla\times\psi\mathbf{e}_\phi,$$
$$\mathbf{j} = j\mathbf{e}_\phi + \nabla\times h\mathbf{e}_\phi.$$

Note that h is the azimuthal component of the induced magnetic field, which is used subsequently instead of Φ for the description of the induced current. Thus we effectively

retain the azimuthal component of the induction equation to describe the meridional components of the induced current, while the azimuthal current is explicitly related to the radial velocity. The use of the electrostatic potential Φ, which provides an alternative mathematical formulation for the induced currents in the inductionless approximation, would result in slightly more complicated governing equations. In addition, for numerical purposes, we introduce an auxiliary variable, vorticity

$$\boldsymbol{\omega} = \boldsymbol{\nabla} \times \mathbf{v} = \omega \mathbf{e}_\phi + \boldsymbol{\nabla} \times v \mathbf{e}_\phi.$$

Perturbation is sought in the normal mode form

$$\{v_1, \omega_1, \psi_1, h_1\}(\mathbf{r},t) = \{\hat{v}, \hat{\omega}, \hat{\psi}, \hat{h}\}(r) \times e^{\gamma t + ikz}, \tag{4}$$

where γ is, in general, a complex growth rate and k is the axial wave number, which is real for the conventional stability analysis and complex when the absolute instability is considered. Henceforth we proceed to dimensionless variables by using $R_i, 1/\Omega_i$, $R_i\Omega_i$, B_0, and $\sigma B_0 R_i \Omega_i$ as the length, time, velocity, magnetic field, and current scales, respectively. The nondimensionalized governing equations read as

$$\gamma \hat{v} = ikr^{-1}(r^2\Omega)'\hat{\psi} + \Lambda ik\hat{h}, \tag{5}$$

$$\gamma \hat{\omega} = 2ik\Omega\hat{v} - \Lambda ik(ik\hat{\psi} + 2\beta r^{-2}\hat{h}), \tag{6}$$

$$0 = D_k\hat{\psi} + \hat{\omega}, \tag{7}$$

$$0 = D_k\hat{h} + ik(\hat{v} - 2\beta r^{-2}\hat{\psi}), \tag{8}$$

where $D_k f \equiv r^{-1}(rf')' - (r^{-2} + k^2)f$ and the prime stands for d/dr; $\Lambda = \sigma B_0^2/\rho\Omega_i$ is the Elsasser number, also referred to as the magnetohydrodynamic interaction parameter, which will be the main dimensionless parameter for the subsequent analysis;

$$\Omega(r) = \frac{\lambda^{-2} - \mu + r^{-2}(\mu - 1)}{\lambda^{-2} - 1} \tag{9}$$

is the dimensionless angular velocity of the base flow defined in terms of $\lambda = R_o/R_i$ and $\mu = \Omega_o/\Omega_i$. Note that Eqs. (5)–(8) are invariant upon the transformations $\{\Omega, k, \hat{h}\} \to -\{\Omega, k, \hat{h}\}$ and $\{\beta, k, \hat{v}\} \to -\{\beta, k, \hat{v}\}$, which means that reversing the direction of rotation Ω or that of helicity β merely inverts the direction in which perturbations propagate along the axis. Similarly, Eqs. (5)–(8) are invariant upon the transformation $(k, \gamma) \to (-k, \gamma^*)$ applied together with the complex conjugate operation, which implies that for a fixed wave number the reversion of Ω or β inverts only the sign of frequency $\omega = \mathrm{Im}[\gamma]$. Owing to these symmetries it suffices to consider only positive β.

In inviscid approximation, the flow perturbation on the inner and outer cylinders at $r = 1$ and $r = \lambda$, respectively, satisfy the impermeability condition $\hat{\psi} = 0$. Boundary conditions for $\hat{h}$ on insulating and perfectly conducting cylinders are $\hat{h} = 0$ and $(r\hat{h})' = 0$, respectively. There are no boundary conditions imposed on the azimuthal velocity perturbation, which is defined in terms of the two previous variables by Eq. (5).

Equations (5)–(8) for perturbation amplitudes were solved in the same way as in Refs. [16,21] using a spectral collocation method based on the Chebyshev-Lobatto grid with a typical number of internal points $N = 32$, which ensured the accuracy of about five digits.

III. NARROW-GAP APPROXIMATION

Before undertaking numerical solution of the whole problem, it is instructive to revisit the local WKB-type solution based on the narrow-gap approximation defined by $\delta = \lambda - 1 \ll 1$, which is the dimensionless gap width between the cylinders. Representing the cylindrical radius as $r = 1 + \delta s$, where s is a local radial coordinate, the angular base flow velocity (9) in Eq. (13) at the leading order in δ becomes $\Omega \approx 1$. The dimensionless radial gradient term of the angular momentum in Eq. (5) can be written for arbitrary gap width as

$$r^{-1}(r^2\Omega)' = 2\frac{\lambda^{-2} - \mu}{\lambda^{-2} - 1} = 2(1 + \mathrm{Ro}), \tag{10}$$

which is constant not only for narrow but also finite-width gap. The latter relation can be used to define the Rossby number for arbitrary gap width as

$$\mathrm{Ro} = \frac{1 - \mu}{\lambda^{-2} - 1}, \tag{11}$$

which for a narrow gap reduces to $\mathrm{Ro} \approx (\mu - 1)/(2\delta) \approx (\ln\sqrt{\Omega})'$. Taking δ as the length scale, which implies the substitutions $\{k, \beta\} \to \{k, \beta\}/\delta$, $\{\hat{\psi}, \hat{h}\} \to \{\hat{\psi}, \hat{h}\}\delta^2$, and $\hat{v} \to \hat{v}\delta$, Eqs. (5)–(8) reduce at the leading order to

$$\gamma \hat{v} = 2ik(1 + \mathrm{Ro})\hat{\psi} + \Lambda ik\hat{h}, \tag{12}$$

$$\gamma \hat{\omega} = 2ik\hat{v} - \Lambda ik(ik\hat{\psi} + 2\beta r^{-2}\hat{h}), \tag{13}$$

$$0 = \hat{\psi}'' - k^2\hat{\psi} + \hat{\omega}, \tag{14}$$

$$0 = \hat{h}'' - k^2\hat{h} + ik(\hat{v} - 2\beta r^{-2}\hat{\psi}), \tag{15}$$

where the prime now stands for d/ds.

A locally periodic solution can be sought in the form $\{\hat{v}, \hat{\psi}, \hat{\omega}, \hat{h}\}(s) = \{\hat{v}_0, \hat{\psi}_0, \hat{\omega}_0, \hat{h}_0\}\sin(ls)$ with constant amplitudes and the radial wave number l. Substituting this into Eqs. (12)–(15) and eliminating the amplitudes yields the dispersion relation

$$4[ik(1 + \mathrm{Ro}) + \beta\Lambda\kappa^2](ik + \beta\Lambda\kappa^2) - (\gamma + \Lambda\kappa^2)[(\gamma + \Lambda\kappa^2)K^2 + 4\beta^2\Lambda\kappa^2] = 0, \tag{16}$$

where $K^2 = k^2 + l^2$ and $\kappa = k/K$.

Although the quadratic equation (16) is easy solvable for the growth rate γ, it is instructive first to consider asymptotic solutions for small and large interaction parameters Λ. In the nonmagnetic case $\Lambda = 0$, the solution is simple:

$$\gamma_0 = \pm 2i\kappa\sqrt{1 + \mathrm{Ro}}, \tag{17}$$

which describes exponentially growing Taylor vortices due to the centrifugal instability when $\mathrm{Ro} < -1$, and constant-amplitude inertial waves when $\mathrm{Ro} \geqslant -1$. For strong interaction at $\Lambda \gg 1$, Eq. (16), reducing to

$$4(\beta\Lambda\kappa^2)^2 - (\gamma + \Lambda\kappa^2)[(\gamma + \Lambda\kappa^2)K^2 + 4\beta^2\Lambda\kappa^2] = 0,$$

yields

$$\gamma = -\Lambda\kappa^2[1 + 2(\beta/K)^2(1 \pm \sqrt{1 + (\beta/K)^{-2}})] < 0, \tag{18}$$

which shows that all perturbations are magnetically damped. For weak interaction at $\Lambda \ll 1$, the growth rate may be sought as a perturbation of the nonmagnetic solution $\gamma \approx \gamma_0 + \Lambda\gamma_1$, where γ_0 is defined by Eq. (17). This expression substituted into Eq. (16) yields

$$\gamma_1 = -K^{-2}\left[k^2 + 2(\beta\kappa)^2 \pm \beta\kappa k\frac{2+\mathrm{Ro}}{\sqrt{1+\mathrm{Ro}}}\right]. \tag{19}$$

According to the above expression, there may be a finite range of helicities bounded by

$$\beta_\pm = \frac{K}{4}\left[\frac{2+\mathrm{Ro}}{\sqrt{1+\mathrm{Ro}}} \pm \sqrt{\frac{(2+\mathrm{Ro})^2}{1+\mathrm{Ro}} - 8}\right], \tag{20}$$

in which inertial waves turn unstable ($\gamma_1 > 0$) however small the interaction parameter Λ. It means that the inviscid HMRI, similarly to its standard counterpart, can be triggered by an arbitrary weak magnetic field provided that its helicity lies in the range defined above. For such an instability range to exist, $\beta_\pm$ has to be real, which, in turn, requires the term under the square root to be non-negative and yields

$$\pm\mathrm{Ro} \geqslant 2\sqrt{2} \pm 2 = \pm\mathrm{Ro}_L^\pm. \tag{21}$$

Taking the plus and minus signs in this expression yields $\mathrm{Ro} \geqslant 2 + 2\sqrt{2} = \mathrm{Ro}_L^+$ and $\mathrm{Ro} \leqslant 2 - 2\sqrt{2} = \mathrm{Ro}_L^-$, respectively, which are originally due to Liu *et al.* [12].

The damping of all perturbations at $\Lambda \gg 1$ following from Eq. (18) implies that instability, if any, is possible only at sufficiently small Λ. The marginal interaction parameter Λ_c, at which perturbations become neutrally stable, is defined by $\mathrm{Re}[\gamma] = 0$. Substituting $\gamma = i\omega$, where ω is the frequency of neutrally stable perturbations, into Eq. (16) and taking the imaginary part, we obtain

$$\omega = \frac{2(2+\mathrm{Ro})\kappa}{K/\beta + 2\beta/K}.$$

This expression substituted into the real part of Eq. (16) results in

$$\Lambda_c = \sqrt{\omega^2/\kappa^2 - 4(1+\mathrm{Ro})} = 2\sqrt{\left(\frac{2+\mathrm{Ro}}{K/\beta + 2\beta/K}\right)^2 - (1+\mathrm{Ro})}. \tag{22}$$

Again, for instability to exist, Λ_c has to be real, which requires the term under the square root to be non-negative. This is equivalent to

$$\frac{(2+\mathrm{Ro})^2}{1+\mathrm{Ro}} \geqslant (K/\beta + 2\beta/K)^2 = f(K/\beta) \geqslant f(\sqrt{2}) = 8,$$

which results in the same constraint as that for $\Lambda \ll 1$ given by Eq. (21). When the condition above is satisfied, instability is confined to the finite wave number band defined by the limiting values,

$$K_\pm = \frac{\beta}{2}\left(\frac{2+\mathrm{Ro}}{\sqrt{1+\mathrm{Ro}}} \pm \sqrt{\frac{(2+\mathrm{Ro})^2}{1+\mathrm{Ro}} - 8}\right) \sim \beta, \tag{23}$$

at which Λ_c in Eq. (22) turns to zero.

These are the basic characteristics of the HMRI in the narrow-gap approximation. It is important to note that although this instability can affect some centrifugally stable velocity distributions with $\mathrm{Ro} > -1$, it does not extend up to the astrophysically relevant Keplerian profile $\Omega \sim r^{-3/2}$, whose Rossby number (11),

$$\mathrm{Ro}_K = -\tfrac{3}{4} > \mathrm{Ro}_L^- \approx -0.828, \tag{24}$$

lies outside the Liu range (21). The aim of the following section is to investigate numerically whether this constraint can be overcome when a finite-width gap is considered.

IV. NUMERICAL RESULTS FOR A FINITE-WIDTH GAP

The numerical results presented in this section are for the gap width between the cylinders equal to the radius of the inner cylinder, which corresponds to $\lambda = R_o/R_i = 2$. The corresponding Rayleigh line is $\mu_R = \Omega_o/\Omega_i = \lambda^{-2} = 0.25$. Above this critical ratio of rotation rates of the inner and outer cylinders the specific angular momentum $r^2\Omega$ turns radially outward increasing and thus the flow becomes hydrodynamically stable with respect to axisymmetric inviscid perturbations.

A. Convective instability

In this section, real wave numbers are considered ($k_i = 0$) as in the standard linear stability analysis, which corresponds to the so-called convective instability. At this threshold, flow becomes able to amplify certain perturbations, which are not necessarily self-sustained and thus may require a permanent external excitation to be observable. For self-sustained perturbations, the absolute instability is required, which is considered in the next section.

The marginal interaction parameters below which the temporal growth rate γ_r becomes positive are shown in Figs. 2 and 3 against the wave number of the corresponding mode for insulating and perfectly conducting boundaries, respectively. For the centrifugally marginal state defined by $\mu = \mu_R$, the neutral stability boundary turns out to be particularly simple: $\Lambda = \beta/k$. The origin of this simple relation is not obvious. Slightly beyond the Rayleigh line ($\mu > 0.25$), the short-wave unstable modes disappear. With the increase in μ, the range of unstable modes rapidly shrinks toward the longer waves. As seen in Fig. 2(a), for sufficiently low helicities β, there is a critical μ at which the long-wave instability mode disappears altogether. For higher β, the instability disappears in a more complex way. As seen in Fig. 2(b) for $\beta = 8$, there is an intermediate-wave mode, which outlasts the long-wave one. This longer lasting mode affects only a limited range of wave numbers, which also quickly shrinks from both ends with the increase in μ. As a result, the range of unstable wave numbers disappears altogether by shrinking to a point at some critical μ, which slightly exceeds that for the disappearance of the long-wave mode discussed above. As seen in Fig. 4, the critical wave number at which this mode disappears increases with the helicity β. Thus this intermediate-wave mode resembles the narrow-gap instability considered in the previous section.

For perfectly conducting boundaries and sufficiently low helicities, the marginal interaction parameter, which is shown in Fig. 3(a) against the wave number for $\beta = 2$, demonstrates a similar variation to that for insulating boundaries seen in

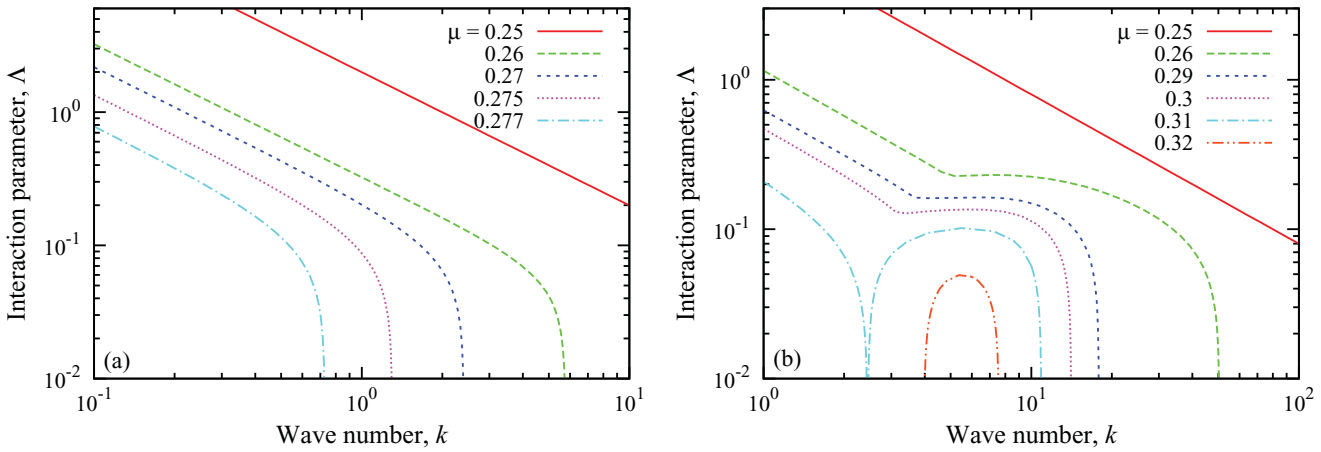

FIG. 2. (Color online) The marginal interaction parameter Λ against the wave number k for the helicities (a) $\beta = 2$ and (b) $\beta = 8$ at different μ; $\Lambda = \beta/k$ at the Rayleigh line $\mu = 0.25$.

Fig. 2(a). In contrast to the insulating boundaries, with the increase in μ, the original long-wave instability mode quickly disappears. What is left behind resembles an intermediate-wave mode for insulating boundaries at high helicities except that the remaining mode extends up to the long-wave limit $k = 0$. In contrast to the original long-wave mode at $\mu = \mu_R$, the marginal interaction parameter for this mode tends to a finite value rather than growing as $\sim k^{-1}$ for $k \to 0$. The main difference from the insulating case is that instability does not vanish at a finite μ. With the increase in μ, instability just shifts to longer waves with the marginal interaction parameter approaching zero, which, as shown in the previous section, implies a similar decrease also in the growth rate. The variation of the marginal interaction parameter for perfectly conducting boundaries at higher helicities is shown in Fig. 3(b) for $\beta = 16$. Slightly beyond the Rayleigh line, instability is due to an intermediate-wave mode, which vanishes at a finite μ similarly to that for the insulating boundaries seen in Fig. 2(b). What is left behind is a long-wave mode, which persists at large μ by shifting to ever longer waves as in the case of low helicities considered above. The above results are summarized in Fig. 4, which shows the extension of instability beyond the Rayleigh line in terms of the marginal wave numbers at which the instability vanishes plotted against the ratio of rotation rates μ for various helicities β.

B. Absolute instability

The convective instability considered in the previous section is not necessarily self-sustained. In spatially unbounded systems, small amplitude perturbations become self-sustained above the absolute instability threshold. In addition to the positive temporal growth rate supposed by the convective instability, the absolute instability requires zero group velocity for the critical perturbation. This additional constraint can be satisfied by a nonzero imaginary part of the wave number $k_i \neq 0$. From a physical as well as computational point of view, it is advantageous to consider the absolute instability as a limiting case of the global instability. The latter supposes that two oppositely propagating modes with the same frequency can be mutually coupled by the reflections from remote end walls. Two such marginal modes having the same imaginary but, generally, different real parts of the wave number can form a neutrally stable global mode with a finite wave packet length

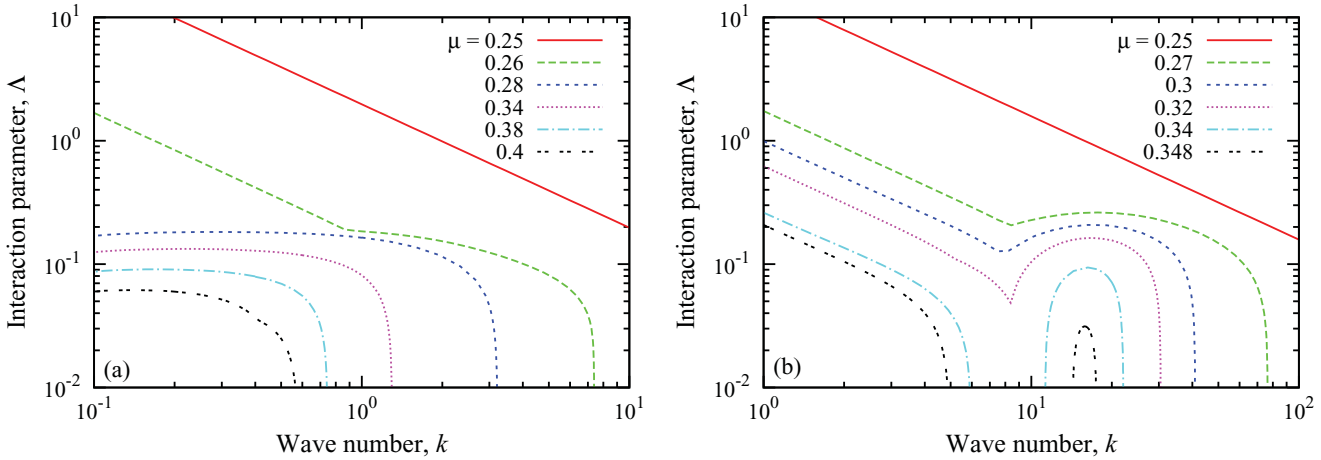

FIG. 3. (Color online) The marginal interaction parameter Λ against the wave number k for the helicities (a) $\beta = 2$ and (b) $\beta = 16$ at different μ; $\Lambda = \beta/k$ at the Rayleigh line $\mu = 0.25$.

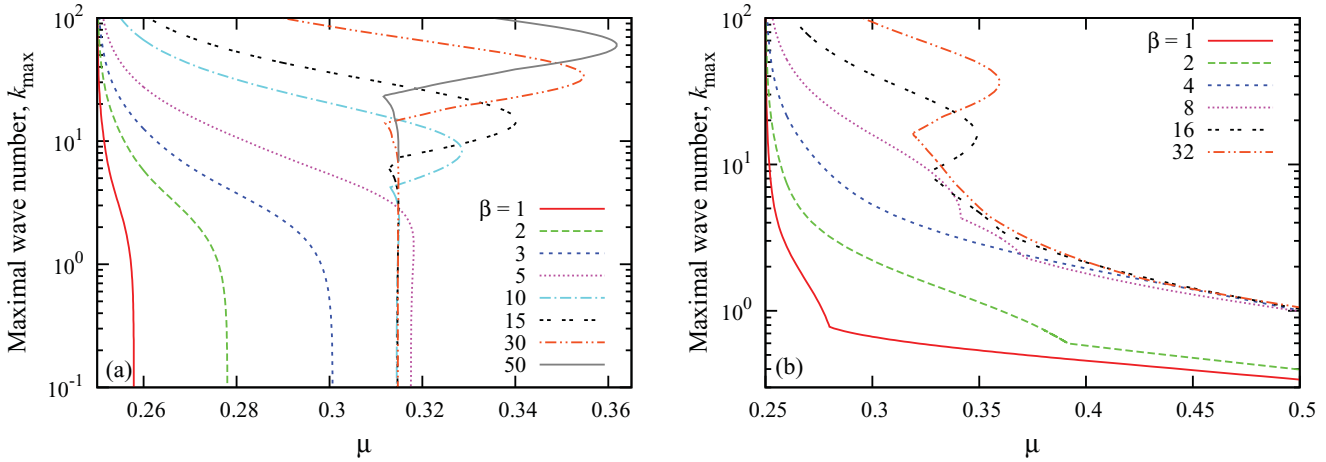

FIG. 4. (Color online) Extension of the HMRI beyond the Rayleigh line ($\mu = 0.25$) for (a) insulating and (b) perfectly conducting boundaries at various helicities β.

fitting in a system of sufficiently large extension [25,26]. The global instability turns into the absolute one when two such oppositely propagating modes merge so that also the real parts of the wave number coincide, which results in a wave packet of infinite extension. This approach will be pursued in the following to locate the absolute instability.

The first step is to consider the neutral stability curves for $k_i \neq 0$ which are plotted in Fig. 5 for insulating boundaries with a rotation rate ratio slightly beyond the Rayleigh line ($\mu = 0.27$) and a moderate helicity $\beta = 5$. As discussed in the previous section, the neutral stability curve for $k_i = 0$, which defines the convective instability threshold, consists of an intermediate- and a long-wave branch. Transition between these branches shows up as a break on the neutral stability curve and as a jump in the associated frequency, which are seen in Figs. 5(a) and 5(b), respectively. For $k_i > 0$ representing the main interest here, both branches merge together and neutral stability curves start to form closed loops, which tighten as k_i is increased. A more relevant information follows from Fig. 5, where the previous two quantities are plotted against each other. It is important to notice that the curves in Fig. 6(b) form not only closed loops but also intersect themselves in a certain range of k_i. For a fixed k_i, the frequencies and the interaction parameters of two modes coincide at the intersection. As discussed above, two such waves could sustain each other by the reflections from the end walls and thus form a marginal global mode provided that they propagate in the opposite directions. The direction of propagation can be determined from the variation of the interaction parameter with k_i. Namely, two modes propagate in the opposite directions if the interaction parameter of one intersecting branch increases while the other decreases with a small variation in k_i [26]. Since this is the case seen in Fig. 6(b), the intersection point defines a marginal interaction parameter for a neutrally stable global mode consisting of two oppositely traveling waves with different real parts of the wave number. At $k_i = 3.80$, the loop below the intersection tightens together forming a cusp. This critical point at which both modes merge together represents the threshold of the absolute instability. Besides the lower threshold there is also an upper one, which occurs at

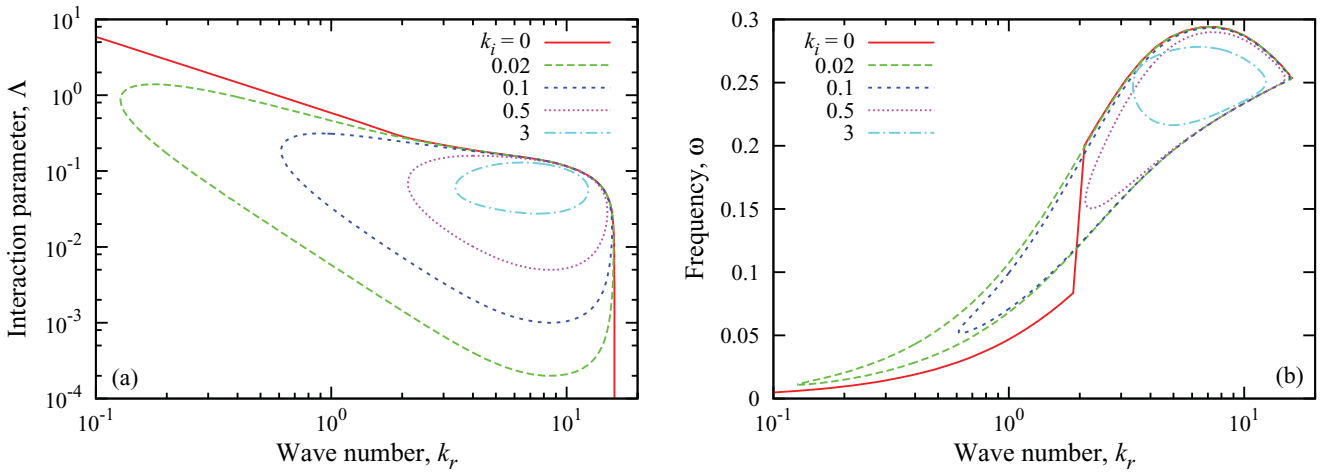

FIG. 5. (Color online) Interaction parameter Λ (a) and the frequency ω (b) for marginally stable modes ($\gamma_r = 0$) versus the real part of the wave number k_r for $\mu = 0.27$ and $\beta = 5$ at various imaginary parts of the wave number k_i.

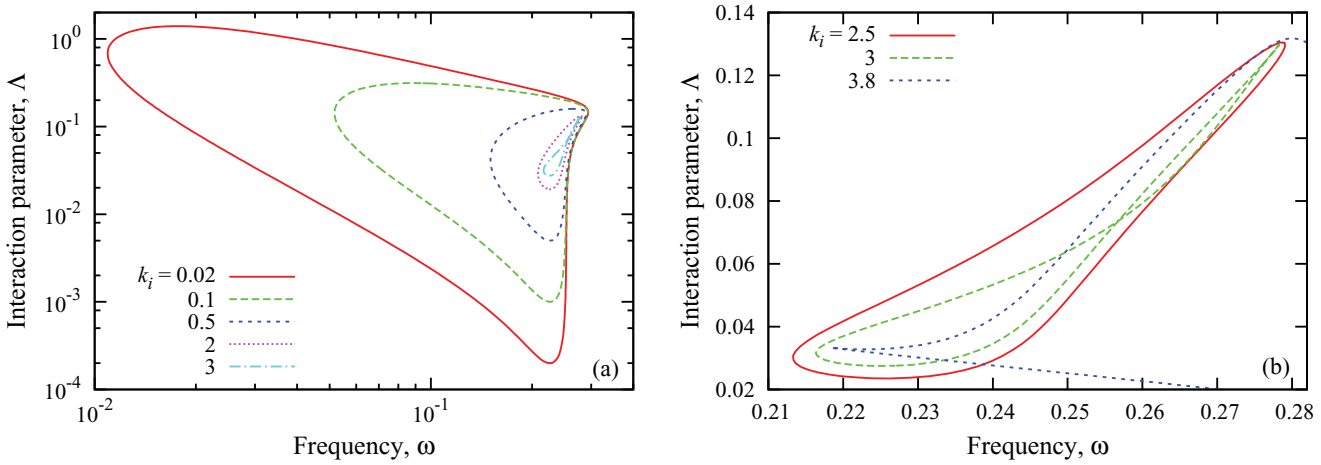

FIG. 6. (Color online) The marginal interaction parameter Λ versus the frequency of neutrally stable modes ω for $\mu = 0.7$ and $\beta = 5$ at various imaginary parts of the wave number k_i.

$k_i = 3.28$ when another cusp forms at the top of the loop. This upper cusp is formed by the second intersection which is hardly noticeable at the upper tip of the loop for $k_i = 3$ in Fig. 6(b).

The thresholds of the absolute instability for insulating boundaries at various helicities are plotted in Fig. 7 against the ratio of rotation rates μ. With increasing the rotation rate or reducing the strength of the magnetic field, the HMRI sets in below the upper critical value of the interaction parameter and vanishes below the lower one, which are shown in Fig. 7(a). Such a double threshold is a characteristic feature of the HMRI that distinguishes it from a magnetically modified Taylor

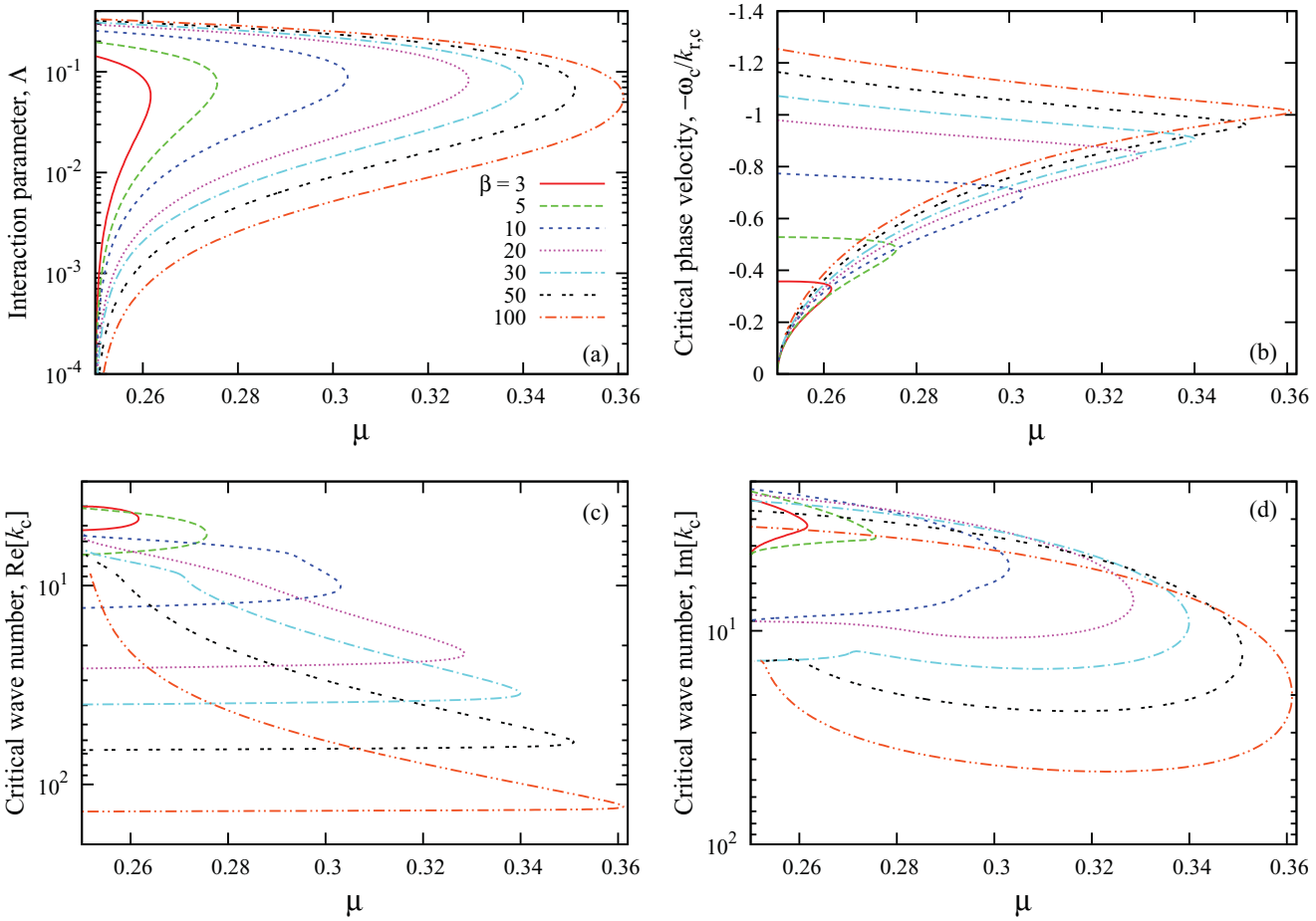

FIG. 7. (Color online) The critical interaction parameter Λ_c (a), the phase velocity (b), the real (c) and imaginary (d) parts of the critical wave number of the absolute instability versus μ for insulating boundaries at various helicities β.

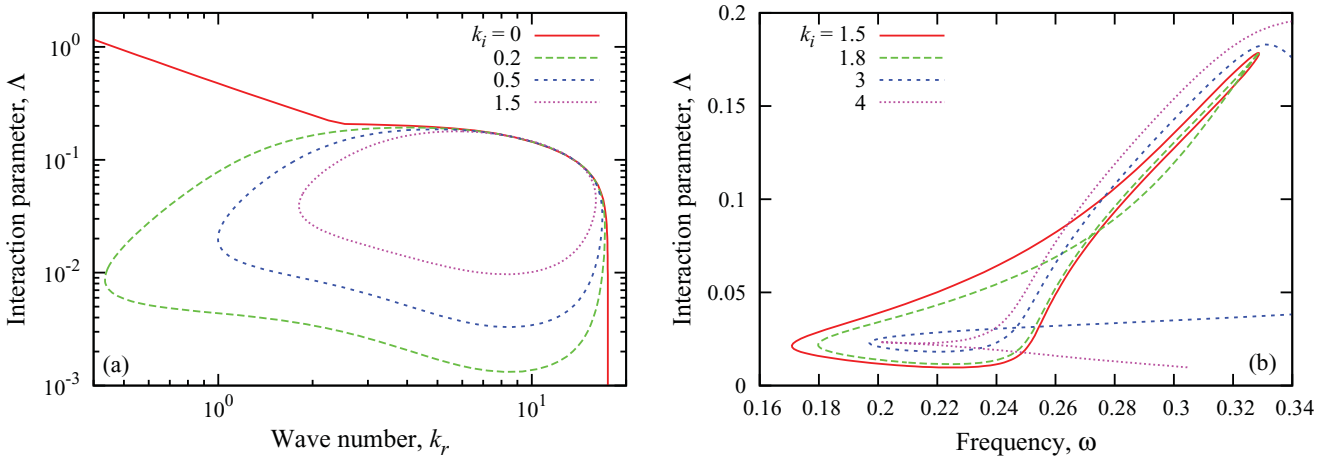

FIG. 8. (Color online) The marginal interaction parameter Λ against the wave number k_r (a) and against the frequency ω (b) for perfectly conducting boundaries at $\mu = 0.27, \beta = 5$, and various k_i.

vortex flow, which exists below the Rayleigh line and has only the upper threshold. The critical phase velocity and the real and imaginary parts of wave number at the instability thresholds are shown in Figs. 7(b)–7(d), respectively. Although the increase of the helicity β makes the instability extend farther beyond the Rayleigh line, the extension is seen in Fig. 9 to saturate at large β.

For the absolute instability, in contrast to the convective one considered in the previous section, there is no significant difference between insulating and perfectly conducting boundaries. For perfectly conducting boundaries, only the intermediate but not the long-wave modes can turn absolutely unstable. As seen in Fig. 8(a), the neutrally stable modes with $k_i > 0$ are limited to finite wave number and interaction parameter ranges. The marginal interaction parameter plotted in Fig. 8(b) against the frequency of neutrally stable modes forms self-intersecting loops as in the case of insulating boundaries shown in Fig. 6(b). Thus the threshold of the absolute instability for perfectly conducting boundaries turns out to be close to that for insulating boundaries shown in Fig. 7.

The proximity of the absolute instability thresholds for insulating and perfectly conducting boundaries is demonstrated in Fig. 9, which shows the extension of the HMRI beyond the Rayleigh line depending on the helicity β. Note that the extension of the convective instability for perfectly conducting boundaries is not shown because it appears unlimited in Fig. 4(b). At high β, the extension of the convective instability for insulating boundaries as well as that of the absolute instability for both insulating and perfectly conducting cylinders are seen to tend to a certain limit of μ. The main question is whether this limit includes the Keplerian velocity profile $\Omega \sim r^{-3/2}$. A simple approximation of the Keplerian profile with the TC one leads to $\mu_\Delta = \lambda^{-3/2} \approx 0.35$ for $\lambda = 2$ under consideration here. As seen in Fig. 9, the HMRI certainly persists beyond this limit. On the other hand, the lower Liu limit (21) substituted into Eq. (11) yields

$$\mu_L = 1 + (1 - \lambda^{-2})\mathrm{Ro}_L^- = \frac{5}{2} - \frac{3}{\sqrt{2}}, \qquad (25)$$

which appears to be the asymptote approached by μ in Fig. 9. It means that the HMRI obeys the Liu limit not only for a thin but also for a finite-width gap. But this obviously contradicts the above conjecture that the HMRI can affect the Keplerian profile, whose Rossby number according to Eq. (24) lies beyond the Liu limit and yields

$$\mu_K = 1 + (1 - \lambda^{-2})\mathrm{Ro}_K = \tfrac{7}{16}. \qquad (26)$$

Indeed, this ratio of rotation rates is seen in Fig. 9 to lie significantly above that for the Liu limit. It is important to note that μ_Δ is an integral criterion based on the difference of angular velocity over the gap width. The velocity difference for the TC profile coinciding with that for the Keplerian profile means that only the average velocity gradients of both profiles are the same. Since the velocity profiles are different, the TC profile will be in some parts of the gap shallower and in some other parts steeper than that of the Keplerian profile [20]. Therefore simple approximation of the Keplerian profile by the TC one based on the total velocity variation may be misleading. This becomes obvious by considering the

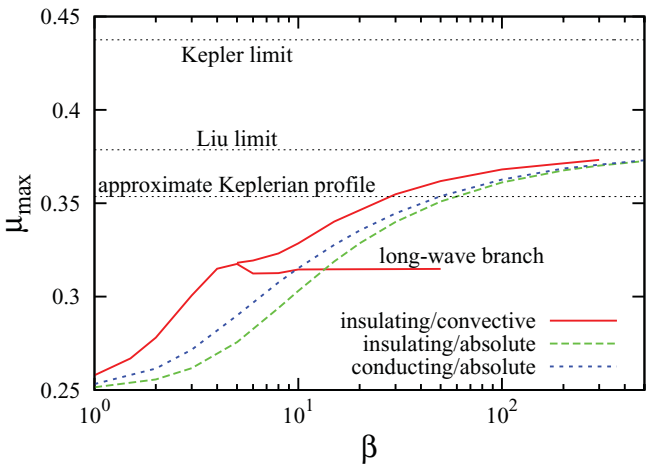

FIG. 9. (Color online) The extension of the convective and absolute HMRI beyond the Rayleigh line versus the helicity β for insulating and perfectly conducting boundaries.

radial gradient term of the specific angular momentum given by Eq. (10), which determines the centrifugal stability. This is also the key parameter for the HMRI, whose critical value is modified by helical magnetic field as shown by the narrow-gap approximation. Expression (10) defines the local slope of the specific angular momentum profile, which is constant for TC flow and can be expressed in terms of either μ or Ro. Then it is easy to see that the slope of TC flow profile corresponding to μ_Δ is indeed considerably lower than the local slope of the Keplerian profile defined by Eq. (26).

V. SUMMARY AND CONCLUSIONS

This paper presented the analysis of the HMRI in the astrophysically relevant limit of a vanishing viscosity. In order to focus on the HMRI, the analysis was carried out in the inductionless approximation defined by zero magnetic Prandtl number $\mathrm{Pm} = 0$, which excludes the standard MRI. These assumptions resulted in the problem defined by a single dimensionless parameter, the Elsasser number, also referred to as the magnetohydrodynamic interaction parameter, which characterizes the ratio of electromagnetic and inertial forces. Using a Chebyshev collocation method convective and absolute instability thresholds were numerically calculated with respect to axisymmetric perturbations of cylindrical TC flow subject to a helical magnetic field. Without the magnetic field, the flow becomes centrifugally unstable when the specific angular momentum of fluid at the inner cylinder exceeds that at the outer one. According to the previous WKB analysis, a strong magnetic field has a stabilizing effect, but a weak field of certain helicity can destabilize some centrifugally stable velocity distributions lying beyond the so-called Rayleigh line. The latter defines the limit of the centrifugal instability in terms of the critical ratio of rotation rates for a given gap width between the cylinders. However, in the WKB approximation, the extension of the instability beyond the Rayleigh line is constrained by the so-called Liu limit and does not reach up to the astrophysically relevant Keplerian velocity profile. The obtained numerical results show that the Liu limit is obeyed also by the nonlocal solution for a finite width gap between the cylinders except for perfectly conducting boundaries. Maximal extension of the absolute HMRI as well as that of the convective HMRI at insulating boundaries is attained when the magnetic field is nearly azimuthal, which produces a short-wave instability as in the WKB approximation. The short-wave character of the instability explains why the nonlocal solution obeys the Liu limit and why it may also apply to other gap widths rather than just the case of $\lambda = 2$ considered in this study. Moreover, the short wavelength implies that the absolute instability, which formally applies to the systems of infinite axial extension, may be relevant also for relatively thin disks. This is because the absolute instability, as discussed at the beginning of Sec. IV B, represents the limit of the global instability with respect to the wave packets of finite length. The wave packets formed by two short waves with slightly different wave numbers can fit in the relatively thin disks.

In the case of perfectly conducting boundaries, the instability can extend sufficiently far beyond the Rayleigh line to reach the astrophysically relevant Keplerian velocity profile. However, this is the case only for the convective instability mode, which is not self-sustained and thus requires an external excitation to be effective. Moreover, as the ratio of rotation rates increases further beyond the Rayleigh line, this instability mode shifts to ever longer waves. First, due to its long wavelength this mode is not only inherently nonlocal but also unable to fit within limited thickness of accretion disks. Second, the critical interaction parameter for this mode approaching zero implies that its growth rate approaches zero too. As a result, this weak instability can be suppressed by a finite viscous damping, which also limits its extension beyond the Rayleigh line [16,21]. Given these three basic constraints, the HMRI at perfectly conduction boundaries seems of a little astrophysical relevance, too.

Note that the Liu limit appears only in the inductionless approximation, which, however, captures the essence of HMRI. At nonzero Pm, instability can extend beyond the Liu limit [8]. Obviously, the HMRI can extend similarly to the SMRI up to the Velikhov-Chandrasekhar limit corresponding to the solid-body rotation. However, this extension is due to the SMRI, in which HMRI merges with at a sufficiently high Reynolds number [27]. For small Pm, the merging point, at which the HMRI loses its identity by turning into the SMRI, is located only slightly above the Liu limit [28]. Thus the HMRI cannot affect the Keplerian velocity profiles even at finite Pm.

[1] E. P. Velikhov, Zh. Éksp. Teor. Fiz. **36**, 1398 (1959) [Sov. Phys. JETP **9**, 995 (1959)].

[2] S. Chandrasekhar, Proc. Nat. Acad. Sci. USA **46**, 253 (1960); *Hydrodynamic and Hydromagnetic Stability*, Sec. 81 (Oxford University, London, 1961).

[3] S. A. Balbus and J. F. Hawley, Astrophys. J. **376**, 214 (1991).

[4] S. A. Balbus and J. F. Hawley, Rev. Mod. Phys. **70**, 1 (1998).

[5] D. R. Sisan, N. Mujica, W. A. Tillotson, Y.-M. Huang, W. Dorland, A. B. Hassam, T. M. Antonsen, and D. P. Lathrop, Phys. Rev. Lett. **93**, 114502 (2004).

[6] H. Ji, M. Burin, E. Schartman, and J. Goodman, Nature (London) **444**, 343 (2006).

[7] J. Goodman and H. Ji, J. Fluid. Mech. **462**, 365 (2002).

[8] R. Hollerbach and G. Rüdiger, Phys. Rev. Lett. **95**, 124501 (2005).

[9] G. Rüdiger, R. Hollerbach, F. Stefani, Th. Gundrum, G. Gerbeth, and R. Rosner, Astrophys. J. **649**, L145 (2006).

[10] F. Stefani, Th. Gundrum, G. Gerbeth, G. Rüdiger, M. Schultz, J. Szklarski, and R. Hollerbach, Phys. Rev. Lett. **97**, 184502 (2006).

[11] F. Stefani, Th. Gundrum, G. Gerbeth, G. Rüdiger, J. Szklarski, and R. Hollerbach, New J. Phys. **9**, 295 (2007).

[12] W. Liu, J. Goodman, I. Herron, and H. Ji, Phys. Rev. E **74**, 056302 (2006).

[13] W. Liu, J. Goodman, and H. Ji, Phys. Rev. E **76**, 016310 (2007).

[14] W. Liu, Phys. Rev. E **77**, 056314 (2008).

[15] W. Liu, Astrophys. J. **692**, 998 (2009).
[16] J. Priede and G. Gerbeth, Phys. Rev. E **79**, 046310 (2009).
[17] J. Priede, Phys. Rev. E **79**, 066314 (2009).
[18] F. Stefani, G. Gerbeth, Th. Gundrum, J. Szklarski, G. Rüdiger, and R. Hollerbach, Astron. Nachr. **329**, 652 (2008).
[19] F. Stefani, G. Gerbeth, Th. Gundrum, R. Hollerbach, J. Priede, G. Rüdiger, and J. Szklarski, Phys. Rev. E **80**, 066303 (2009).
[20] G. Rüdiger and R. Hollerbach, Phys. Rev. E **76**, 068301 (2007).
[21] J. Priede, I. Grants, and G. Gerbeth, Phys. Rev. E **75**, 047303 (2007).
[22] P. H. Roberts, *An Introduction to Magnetohydrodybamics*, Sec. 2.1 (Longmans, London, 1967).
[23] G. Rüdiger, R. Hollerbach, M. Schultz, and D. A. Shalybkov, Astron. Nachr. **326**, 409 (2005).
[24] R. Hollerbach, V. Teeluck, and G. Rüdiger, Phys. Rev. Lett. **104**, 044502 (2010).
[25] E. M. Lifshitz and L. P. Pitaevskii, *Physical Kinetics*, Secs. 62 and 65 (Pergamon, London, 1981).
[26] J. Priede and G. Gerbeth, Phys. Rev. E **56**, 4187 (1997).
[27] O. N. Kirillov and F. Stefani, Astrophys. J. **712**, 52 (2010).
[28] O. N. Kirillov and F. Stefani, Phys. Rev. E **84**, 036304 (2011).